Study with Agonist Ligand [11c]MNPA, Brain'09 & BrainPET'09, Chicago, 2009.06

11. Hiroyuki Takuwa, Kazuto Masamoto, Takayuki Obata, Iwao Kanno: Dynamic recording of ongoing neurovascular activity in awake-behaving mice., XXIVth International Symposium on Cerebral Blood Flow, Metabolism and Function & VIth International Conference on Quantification of Brain Function with PET, Chicago, 2009.06

12. Hiroyuki Takuwa, Tetsuya Matsuura, Rumiana Bakalova-Zheleva, Takayuki Obata, Iwao Kanno: Nitric Oxide as a Major Mediator of Neurovascular Coupling in Hypoxia: Free Radical Hypothesis, XXIVth International Symposium on Cerebral Blood Flow, Metabolism and Function & VIth International Conference on Quantification of Brain Function with PET, Chicago, 2009.06

13. Yuichi Kimura, Chie Seki, Hashizume Nobuya, Takahiro Nishimoto*, Keishi Kitamura, Iwao Kanno: Development of Microfluidic Plasma Counting System for Small Animal Molecular Imaging Using PET --- Measurement of Small Radioactivity Concentration, 2009 World Molecular Imaging Congress, Montreal, 2009.09

14. 松浦　哲也、田桑　弘之、バカロバ　ルミアナ、小畠　隆行、菅野　巖: ラット脳賦活血流量の調節におけるCOX-2の関与、日本動物学会第８０回大会、静岡市、2009.09

15. 菅野　巖: 「脳分子イメージングの最近の動向」および「脳血管障害におけるＰＥＴの貢献と期待」についての討論、「脳分子イメージングの最近の動向」および「脳血管障害におけるＰＥＴの貢献と期待」についての討論、大阪、2009.08

## G．知的財産権の出願・登録状況（予定を含む。）

1. 特許取得

出願日：2009年9月30日
出願番号：2009-227513
名称：遠心分離装置
共同出願者：木村裕一、関千江、菅野巖、橋爪宣弥、北村圭司、西本尚弘
（放医研と島津製作所との共同出願）

2. 実用新案登録

特になし

# III. 研究成果の刊行に関する一覧表

研究成果の刊行に関する一覧表

書籍

| 著者氏名 | 論文タイトル名 | 書籍全体の編集者名 | 書　籍　名 | 出版社名 | 出版地 | 出版年 | ページ |
|---|---|---|---|---|---|---|---|
| 寺本　昇 | 動物実験手技集成 | | 動物実験手技集成 | N.T.S | 日本 | 2009 | 1-62 |

雑誌

| 発表者氏名 | 論文タイトル名 | 発表誌名 | 巻号 | ページ | 出版年 |
|---|---|---|---|---|---|
| Koshino K, Watabe H, Hasegawa S, Hayashi T,Hatazawa J, Iida H | Development of motion correction techniquefor cardiac $^{15}$O-water PET study using an opticalmot-ion trackingsystem | *Ann Nucl Med* | 24 | 1-11 | 2010 |
| Temma T, Iida H, Hayashi T, Teramoto N, Ohta Y,Kudomi N, Watabe H, Saji H, Magata Y. | Quantification of Regional Myocardial Oxygen Metabolism in Normal Pigs using Positron Emission Tomography with Injectable $^{15}O$-$O_2$ | *Eur J Nucl Med Mol Imaging* | 37 | 377-385 | 2010 |
| Ikoma Y, Watabe H, Hayashi T, Miyake Y, Teramoto N, Minato K, Iida H | Measurement of Density and Affinity for Dopamine$D_2$ Receptors by a Single PET Scan with Multiple Injections of [$^{11}$C]raclopride | *J Cereb Blood Flow Metab* | 30 | 663-673 | 2010 |
| 飯田秀博, 銭谷勉, 越野一博, 平野祥之 | 核医学的測定法の進歩 | *分子脳血管病* | 9 | 44-50 | 2010 |
| 崎本智則, 銭谷勉, 石田健二, 渡部浩司, 平野祥之, Antti Sohlberg, 湊小太郎, 飯田秀博 | 頭部SPECTにおけるコリメータ開口補正およびモンテカルロ法に基づく散乱線補正を用いた画像再構成法の定量精度評価 | *日本医用画像工学会誌*<br>*Medical Imaging Technology* | 28 | 135-144 | 2010 |
| Yokoyama,M. | Polymeric micelles as a novel drug carrier system and their required consid-erations for clinical trials | *Expert Opinion on Drug Delivery* | 7 | 145-158 | 2010 |
| 横山昌幸 | 高分子ミセルの薬剤学分野への応用 | *薬剤学* | 70 | 27-31 | 2010 |

| | | | | | |
|---|---|---|---|---|---|
| Hori, K., Nishihara, M., and Yokoyama, M. | Vital microscopic analysis of polymeric micelle extravasation from tumor vessels: macromolecular delivery according to tumor vascular growth stage | *J. Pharm. Sci.* | 99 | 549-562 | 2010 |
| Ma,H., Shiraishi, K., Yokoyama, M., Maitani, Y., et al. | Accelerated Blood Clearance Was Not Induced for a Gadolinium- Containing PEG-poly(L-lysine)-Based Polymeric Micelle in Mice | *Pharmaceutical Research* | 27 | 296-302 | 2010 |
| Hori, K., Nishihara, M., and Yokoyama, M. | The Combretastatin Derivative Cderiv, a Vascular Disrupting Agent, Enables Polymeric Nanomicelles to Accumulate in Microtumors | *J. Pharm. Sci.* | | | in press |
| 工藤博幸, イサムラシド | インテリアＣＴにおける画像再構成法の提案 | *映像情報メディカル* | 41 | 1341-1347 | 2010 |
| 工藤博幸 | ＭＲＩ情報を用いた脳血流ＳＰＥＣＴ画像の解析と再構成 | *日本医用画像工学会誌 Medical Imaging Technology* | 28 | 19-25 | 2010 |
| Masamoto K, Obata T, Kanno I | Intracortical microcirculatory change induced by anesthesia in rat somatosensory cortex | *Adv Exp Med Biol* | 662 | 57-61 | 2010 |
| Shidahara M, Ito H, Otsuka T, Ikoma Y, Arakawa R, Kodaka F, Seki C, Takano H, Takahashi H, Turkheimer FE, Kimura Y, Kanno I, Suhara T | Measurement error analysis for the determination of dopamine $D_2$ receptor occupancy using the agonist radioligand [$^{11}$C]MNPA | *J Cereb Blood Flow Metab* | 30 | 187-195 | 2010 |
| N Kudomi, MJ Järvisalo, J Kiss, R Borra, A Viljanen, T Viljanen, TSavunen,J Knuuti, H Iida, P Nuutila,P Iozzo | Non-invasive estimation of hepatic glucose uptake from [$^{18}$F]FDG PET imageusing tissue-derived input functions | *Eur J Nucl Med Mol Imaging* | | in press | 2009 |
| Kudomi N, Koivuviita N, Liukko KE, Oikonen VJ, Tolvanen T, Iida H, TerttiR, Metsarinne K, Iozzo P,Nuutila P | Parametric renal blood flow imaging using [$^{15}$O]$H_2O$ and PET | *Eur J Nucl Med Mol Imaging* | 36(4) | 683-691 | 2009 |
| Yamamoto A, Sato H, Enmi J, Ishida K, Ose T, Kimura A, FujiwaraH, Watabe H, Hayashi T, Iida H. | Use of clinical MRI scanner for pre-clinical researchon rats | *Radiological Physics and Technology* | 2 | 13-21 | 2009 |

| | | | | | |
|---|---|---|---|---|---|
| Kudomi N, Hayashi T, Watabe H, Teramoto N, Piao R, Ose T, Koshino K, Ohta Y, Iida H | A physiological model for recirculation water correction in $CMRO_2$ assessment with $^{15}O_2$ inhalation PET | *J Cereb Blood Flow Metab* | 29 | 355-364 | 2009 |
| Iihara K, Okawa M, Hishikawa T, Yamada N, Fukushima K, Iida H, MiyamotoS | Slowly progressive neuronal death associated with postischemic hyperperfusion in cortical laminar necrosis after high-flow bypass for a carotid intracavernous aneurysm | *J Neurosurg* | | in press | 2009 |
| Iwanishi K, Watabe H, Hayashi T, Miyake Y, Minato K, Iida H | Influence of residual oxygen-15-labeled carbon monoxide radioactivity on cerebral blood flow and oxygen extraction fraction in adual-tracer autoradiographic method | *Ann Nucl Med* | 23 | 363-371 | 2009 |
| Ikoma Y, Watabe H, Hayashi T, Miyake Y, Teramoto N, Minato K, Iida H | Quantitative evaluation of changes in binding potential with a simplified reference tissue model and multiple injections of [$^{11}$C]raclopride | *Neuroimage* | 47 | 1639-1648 | 2009 |
| Iwanishi K, Watabe H, Fujisaki H, Hayashi T, Miyake Y, Minato K, Naganuma M, Uehara T, Yokota C, Moriwaki H, Kajimoto K, Fukushima K, Minematsu K, Iida H | Evaluation of utility of asymmetric index for count-based oxygen extraction fraction on dual-tracer autoradiographic method for chronic unilateral brain infarction | *Ann Nucl Med* | 23 | 533-539 | 2009 |
| Yamanami M, Yamamoto A, Iida H, Watanabe T, Kanda K, Yaku H, Nakayama Y | 3-Tesla magnetic resonance angiographic assessment of a tissue-engineered small-caliber vascular graft implanted in a rat | *J Biomed Mater Res B Appl Biomater* | 92B | 156-160 | 2009 |
| Zeniya T, Hirano Y, Sakimoto T, Ishida K, WatabeH, Teramoto N, Kudo H, Minato K, Hatazawa J, Iida H | Conceptual design of high resolution and quantitative SPECT system for imaging a selected small ROI of human brain | *2009 IEEE Nuclear Science Symposium ConferenceRecord* | | 3484-3486 | 2009 |
| Hirano Y, Zeniya T, Watabe H, Iida H | Performance estimation of high resolution SPECT for the human brain by Monte Carlo simulation of scintillation lights | *2009 IEEE Nuclear Science Symposium Conference Record* | | 3602-3605 | 2009 |

| | | | | | |
|---|---|---|---|---|---|
| Huang Q, Zeniya T, Kudo H, Iida H, Gullberg G | Interior SPECT reconstruct-ion problem with tiny a priori knowledge -An application for high resolution pinhole brain imaging | *Proceedings of 10th InternationalMeeting on FullyThree-Dimensional Image Reconstruction in Radiology and Nuclear Medicine* | | 358-361 | 2009 |
| de Jong HW, Lubberink M, Watabe H, Iida H, Lammertsma AA | A method to measure PET scatter fractions for daily quality control | *Med Phys* | 36 | 4609-4615 | 2009 |
| Inoue, T., Yamashita, Y., Yokoyama, M., Tominaga, T., et al. | Therapeutic efficacy of a polymeric micellar doxorubicin infused by convection- enhanced delivery against intracranial 9L brain tumor models | *Neuro-Oncology* | 11 | 151-157 | 2009 |
| Shiraishi, K., Maitani,Y., Yokoyama, M., et al., | Preparation and in vivo imaging of PEG-poly (L-lysine)-based polymeric micelle MRI contrast agents, | *J. Controlled Release* | 136 | 14-20 | 2009 |
| Okuda, T., Kawakami, S., Yokoyama, M., Hashida, M., et al. | Enhanced in vivo antitumor efficacy of fenretinide encapsulated in polymeric micelles | *Int. J. Pharm.* | 373 | 100-106 | 2009 |
| Murakami, Y., Yokoyama, M., et al. | In Vivo and In Vitro Evaluation of Gelation and Hemostatic Properties of a Novel Tissue-Adhesive Hydrogel Containing a Crosslinkable Polymeric Micelle | *J. Biomed. Mater. Res.: Part B* | 91 | 102-108 | 2009 |
| Kawaguchi, T., Yokoyama, M., et al. | Histological study on side effects and tumor targeting of a block copolymer micelle on rats | *J. Controlled Release* | 136 | 240-246 | 2009 |
| Satoh, T., Shudo, K., Yokoyama, M., et al. | Encapsulation of the synthetic retinoids Am80 and LE540 into polymeric micelles and the retinoids' release | *J. Controlled Release* | 136 | 187-195 | 2009 |

| | | | | | |
|---|---|---|---|---|---|
| Nishihara, M., Imai, K., and Yokoyama, M. | Preparation of Perfluoro-carbon/ Fluoroalkyl Polymer Nanodroplets for Cancer-targeted Ultrasound Contrast Agents | *Chemistry Letters* | 38 | 556-557 | 2009 |
| 横山昌幸 | ＤＤＳと分子イメージング：ＭＲＩ造影剤を例にして | *JSMI Report* | 2 | 9-11 | 2009 |
| 横山昌幸 | ＤＤＳと分子イメージング | *血管医学* | 10 | 97-104 | 2009 |
| 横山昌幸 | 自己組織化高分子のターゲティングへの応用 | *高分子* | 58 | 469-472 | 2009 |
| Minowa, T., Shiraishi, K., Yokoyama, M., Maitani, Y., et al. | Increase in tumour permeability following TGF-b type I receptor inhibitor treatment observed by dynamic contrast - enhanced MRI | *Br. J. Cancer* | 101 | 1884-1890 | 2009 |
| E.A.Rashed, H.Kudo | Intensity-based Bayesian framework for image reconstruction from sparse projection data | *日本医用画像工学会誌 Medical Imaging Technology* | 27 | 243-251 | 2009 |
| E.A.Rashed, H.Kudo, F.Noo | Iterative region-of-interest reconstruction from truncated CT projection data under blind object support | *日本医用画像工学会誌 Medical Imaging Technology* | 27 | 321-331 | 2009 |
| Zhelev Z, Bakalova R, Aoki I, Matsumoto K, Gadjeva V, Anzai K, Kanno I | Nitroxyl radicals for labeling of conventional therapeutics and noninvasive magnetic resonance imaging of their permeability for blood-brain barrier: relationship between structure, blood clearance, and MRI signal dynamic in the brain. | *Mol Pharm* | 6 | 504-512 | 2009 |
| Matsuura T, Takuwa H, Bakalova R, Obata T, Kanno I | Effect of cyclooxygenase-2 on the regulation of cerebral blood flow during neuronal activation in the rat | *Neurosci Res* | 65 | 64-70 | 2009 |
| Kershaw J, Tomiyasu M, Kashikura K, Hirano Y, Nonaka H, Hirano M, Ikehira H, Kanno I, Obata T | A multi-compartmental SE-BOLD interpretation for stimulus-related signal changes in diffusion-weighted functional MRI | *NMR Biomed* | 22 | 770-778 | 2009 |

| | | | | | |
|---|---|---|---|---|---|
| Kawamura K, Yamasaki T, Yui J, Hatori A, Konno F, Kumata K, Irie T, Fukumura T, Suzuki K, Kanno I, Zhang MR. | In vivo evaluation of P-glycoprotein and breast cancer resistance protein modulation in the brain using [$^{11}$C]gefitinib | *Nucl Med Biol* | 36 | 239-246 | 2009 |
| Matsubara S, Moroi J, Suzuki A, Sasaki M, Nagata K, Kanno I, Miura S | Analysis of cerebral perfusion and metabolism assessed with positron emission tomography before and after carotid artery stenting | *J Neurosurg* | 111 | 28-36 | 2009 |
| Shidahara M, Seki C, Naganawa M, Sakata M, Ishikawa M, Ito H, Kanno I, Ishiwata K, Kimura Y | Improvement of likelihood estimation in Logan graphical analysis using maximum a posteriori for neuroreceptor PET imaging | *Ann Nucl Med* | 23 | 163-171 | 2009 |

# Ⅳ．研究成果の刊行物・別刷

# INDEX

【書籍】

| 著者氏名 | 書籍名 | ページ |
|---|---|---|
| 寺本　昇 | 動物実験手技集成 | 364 |

【雑誌】

| 発表者氏名 | 論文タイトル名 | 発表誌名 | ページ |
|---|---|---|---|
| Koshino K, Watabe H, Hasegawa S, Hayashi T, Hatazawa J, Iida H | Development of motion correction technique for cardiac $^{15}$O-water PET study using an optical motion tracking system | *Ann Nucl Med* | 1 |
| Temma T, Iida H, Hayashi T, Teramoto N, Ohta Y,Kudomi N, Watabe H, Saji H, Magata Y. | Quantification of Regional Myocardial Oxygen Metabolism in Normal Pigs using Positron Emission Tomography with Injectable $^{15}$O-$O_2$ | *Eur J Nucl Med Mol Imaging* | 12 |
| Ikoma Y, Watabe H, Hayashi T, Miyake Y, Teramoto N, Minato K, Iida H | Measurement of Density and Affinity for Dopamine$D_2$ Receptors by a Single PET Scan with Multiple Injections of [$^{11}$C]raclopride | *J Cereb Blood Flow Metab* | 21 |
| 飯田秀博, 銭谷勉, 越野一博, 平野祥之 | 核医学的測定法の進歩 | *分子脳血管病* | 32 |
| 崎本智則, 銭谷勉, 石田健二, 渡部浩司, 平野祥之, Antti Sohlberg, 湊小太郎, 飯田秀博 | 頭部SPECTにおけるコリメータ開口補正およびモンテカルロ法に基づく散乱線補正を用いた画像再構成法の定量精度評価 | *日本医用画像工学会誌 Medical Imaging Technology* | 39 |
| Yokoyama,M. | Polymeric micelles as a novel drug carrier system and their required considerations for clinical trials | *Expert Opinion on Drug Delivery* | 49 |
| 横山昌幸 | 高分子ミセルの薬剤学分野への応用 | *薬剤学* | 63 |
| Hori, K., Nishihara, M., and Yokoyama, M. | Vital microscopic analysis of polymeric micelle extravasation from tumor vessels: macromolecular delivery according to tumor vascular growth stage | *J. Pharm. Sci.* | 67 |
| Ma,H., Shiraishi, K., Yokoyama, M., Maitani, Y., et al. | Accelerated Blood Clearance Was Not Induced for a Gadolinium-Containing PEG-poly(L-lysine)-Based Polymeric Micelle in Mice | *Pharmaceutical Research* | 81 |
| Hori, K., Nishihara, M., and Yokoyama, M. | The Combretastatin Derivative Cderiv, a Vascular Disrupting Agent, Enables Polymeric Nanomicelles to Accumulate in Microtumors | *J. Pharm. Sci.* | 88 |
| 工藤博幸, イサムラシド | インテリアＣＴにおける画像再構成法の提案 | *映像情報メディカル* | 100 |
| 工藤博幸 | ＭＲＩ情報を用いた脳血流ＳＰＥＣＴ画像の解析と再構成 | *日本医用画像工学会誌 Medical Imaging Technology* | 107 |

| | | | |
|---|---|---|---|
| Masamoto K, Obata T, Kanno I | Intracortical microcirculatory change induced by anesthesia in rat somatosensory cortex | *Adv Exp Med Biol* | 114 |
| Shidahara M, Ito H, Otsuka T, Ikoma Y, Arakawa R, Kodaka F, Seki C, Takano H, Takahashi H, Turkheimer FE, Kimura Y, Kanno I, Suhara T | Measurement error analysis for the determination of dopamine $D_2$ receptor occupancy using the agonist radioligand [$^{11}$C]MNPA | *J Cereb Blood Flow Metab* | 120 |
| N Kudomi, MJ Järvisalo, J Kiss, R Borra, A Viljanen, T Viljanen, TSavunen,J Knuuti, H Iida, P Nuutila,P Iozzo | Non-invasive estimation of hepatic glucose uptake from [$^{18}$F]FDG PET image using tissue-derived input functions | *Eur J Nucl Med Mol Imaging* | 129 |
| Kudomi N, Koivuviita N, Liukko KE, Oikonen VJ, Tolvanen T, Iida H, TerttiR, Metsarinne K, Iozzo P,Nuutila P | Parametric renal blood flow imaging using [$^{15}$O]$H_2O$ and PET | *Eur J Nucl Med Mol Imaging* | 142 |
| Yamamoto A, Sato H, Enmi J, Ishida K, Ose T, Kimura A, FujiwaraH, Watabe H, Hayashi T, Iida H. | Use of clinical MRI scanner for pre-clinical researchon rats | *Radiological Physics and Technology* | 151 |
| Kudomi N, Hayashi T, Watabe H, Teramoto N, Piao R, Ose T, Koshino K, Ohta Y, Iida H | A physiological model for recirculation water correct- ion in $CMRO_2$ assessment with $^{15}O_2$ inhalation PET | *J Cereb Blood Flow Metab* | 160 |
| Iihara K, Okawa M, Hishikawa T, Yamada N, Fukushima K, Iida H, Miyamoto S | Slowly progressive neuronal death associated with postischemic hyperperfusion in cortical laminar necrosis after high-flow bypass for a carotid intracavernous aneurysm | *J Neurosurg* | 170 |
| Iwanishi K, Watabe H, Hayashi T, Miyake Y, Minato K, Iida H | Influence of residual oxygen-15-labeled carbon monoxide radioactivity on cerebral blood flow and oxygen extraction fraction in a dual-tracer autoradio- graphic method | *Ann Nucl Med* | 176 |
| Ikoma Y, Watabe H, Hayashi T, Miyake Y, Teramoto N, Minato K, Iida H | Quantitative evaluation of changes in binding potential with a simplified reference tissue model and multiple injections of [$^{11}$C]raclopride | *Neuroimage* | 185 |
| Iwanishi K, Watabe H, Fujisaki H, Hayashi T, Miyake Y, Minato K, Naganuma M, Uehara T, Yokota C, Moriwaki H, Kajimoto K, Fukushima K, Minematsu K, Iida H | Evaluation of utility of asymmetric index for count- based oxygen extraction fraction on dual-tracer autoradiographic method for chronic unilateral brain infarction | *Ann Nucl Med* | 195 |
| Yamanami M, Yamamoto A, Iida H, Watanabe T, Kanda K, Yaku H, Nakayama Y | 3-Tesla magnetic resonance angiographic assessment of a tissue-engineered small- caliber vascular graft implanted in a rat | *J Biomed Mater Res B Appl Biomater* | 202 |
| Zeniya T, Hirano Y, Sakimoto T, Ishida K, WatabeH, Teramoto N, Kudo H, Minato K, Hatazawa J, Iida H | Conceptual design of high resolution and quantitative SPECT system for imaging a selected small ROI of human brain | *2009 IEEE Nuclear Science Symposium ConferenceRecord* | 207 |
| Hirano Y, Zeniya T, Watabe H, Iida H | Performance estimation of high resolution SPECT for the human brain by Monte Carlo simulation of scintillation lights | *2009 IEEE Nuclear Science Symposium Conference Record* | 210 |

| | | | |
|---|---|---|---|
| Huang Q, Zeniya T, Kudo H, Iida H, Gullberg G | Interior SPECT reconstruct- ion problem with tiny a priori knowledge -An application for high resolution pinhole brain imaging | *Proceedings of 10th InternationalMeeting on FullyThree-Dimensional Image Reconstruction in Radiology and Nuclear Medicine* | 214 |
| de Jong HW, Lubberink M, Watabe H, Iida H, Lammertsma AA | A method to measure PET scatter fractions for daily quality control | *Med Phys* | 218 |
| Inoue, T., Yamashita, Y., Yokoyama, M., Tominaga, T., et al. | Therapeutic efficacy of a polymeric micellar doxorubicin infused by convection- enhanced delivery against intracranial 9L brain tumor models | *Neuro-Oncology* | 225 |
| Shiraishi, K., Maitani,Y., Yokoyama, M., et al., | Preparation and in vivo imaging of PEG-poly (L-lysine)-based polymeric micelle MRI contrast agents | *J. Controlled Release* | 232 |
| Okuda, T., Kawakami, S., Yokoyama, M., Hashida, M., et al. | Enhanced in vivo antitumor efficacy of fenretinide encapsulated in polymeric micelles | *Int. J. Pharm.* | 239 |
| Murakami, Y., Yokoyama, M., et al. | In Vivo and In Vitro Evaluation of Gelation and Hemostatic Properties of a Novel Tissue-Adhesive Hydrogel Containing a Crosslinkable Polymeric Micelle | *J. Biomed. Mater. Res.: Part B* | 246 |
| Kawaguchi, T., Yokoyama, M., et al. | Histological study on side effects and tumor targeting of a block copolymer micelle on rats | *J. Controlled Release* | 253 |
| Satoh, T., Shudo, K., Yokoyama, M., et al. | Encapsulation of the synthetic retinoids Am80 and LE540 into polymeric micelles and the retinoids' release | *J. Controlled Release* | 260 |
| Nishihara, M., Imai, K., and Yokoyama, M. | Preparation of Perfluoro- carbon/ Fluoroalkyl Polymer Nanodroplets for Cancer-targeted Ultrasound Contrast Agents | *Chemistry Letters* | 269 |
| 横山昌幸 | ＤＤＳと分子イメージング:ＭＲＩ造影剤を例にして | *JSMI Report* | 271 |
| 横山昌幸 | ＤＤＳと分子イメージング | *血管医学* | 274 |
| 横山昌幸 | 自己組織化高分子のターゲティングへの応用 | *高分子* | 282 |
| Minowa, T., Shiraishi, K., Yokoyama, M., Maitani, Y., et al. | Increase in tumour permeability following TGF-b type I receptor inhibitor treatment observed by dynamic contrast - enhanced MRI | *Br. J. Cancer* | 286 |
| E.A.Rashed, H.Kudo | Intensity-based Bayesian framework for image reconstruction from sparse projection data | *日本医用画像工学会誌 Medical Imaging Technology* | 293 |
| E.A.Rashed, H.Kudo, F.Noo | Iterative region-of-interest reconstruction from truncated CT projection data under blind object support | *日本医用画像工学会誌 Medical Imaging Technology* | 302 |

| | | | |
|---|---|---|---|
| Zhelev Z, Bakalova R, Aoki I, Matsumoto K, Gadjeva V, Anzai K, Kanno I | Nitroxyl radicals for labeling of conventional therapeutics and noninvasive magnetic resonance imaging of their permeability for blood-brain barrier: relationship between structure, blood clearance, and MRI signal dynamic in the brain. | *Mol Pharm* | 313 |
| Matsuura T, Takuwa H, Bakalova R, Obata T, Kanno I | Effect of cyclooxygenase-2 on the regulation of cerebral blood flow during neuronal activation in the rat | *Neurosci Res* | 322 |
| Kershaw J, Tomiyasu M, Kashikura K, Hirano Y, Nonaka H, Hirano M, Ikehira H, Kanno I, Obata T | A multi-compartmental SE-BOLD interpretation for stimulus-related signal changes in diffusion-weighted functional MRI | *NMR Biomed* | 329 |
| Kawamura K, Yamasaki T, Yui J, Hatori A, Konno F, Kumata K, Irie T, Fuku- mura T, Suzuki K, Kanno I, Zhang MR. | In vivo evaluation of P-glycoprotein and breast cancer resistance protein modulation in the brain using [$^{11}$C]gefitinib | *Nucl Med Biol* | 338 |
| Matsubara S, Moroi J, Suzuki A, Sasaki M, Nagata K, Kanno I, Miura S | Analysis of cerebral perfusion and metabolism assessed with positron emission tomography before and after carotid artery stenting | *J Neurosurg* | 346 |
| Shidahara M, Seki C, Naganawa M, Sakata M, Ishikawa M, Ito H, Kanno I, Ishiwata K, Kimura Y | Improvement of likelihood estimation in Logan graphical analysis using maximum a posteriori for neuroreceptor PET imaging | *Ann Nucl Med* | 355 |

Ann Nucl Med (2010) 24:1–11
DOI 10.1007/s12149-009-0323-8

ORIGINAL ARTICLE

# Development of motion correction technique for cardiac $^{15}$O-water PET study using an optical motion tracking system

**Kazuhiro Koshino · Hiroshi Watabe · Shinji Hasegawa · Takuya Hayashi · Jun Hatazawa · Hidehiro Iida**

Received: 19 August 2009 / Accepted: 9 October 2009 / Published online: 3 December 2009


**Abstract**
*Objective* Cardiac $^{15}$O-water PET studies provide an accurate quantitation of regional myocardial blood flow (rMBF). We developed a motion correction system using an optical motion-tracking device to detect a subject's global movement for cardiac study.
*Methods* PET studies were carried out on a cardiac phantom and a healthy volunteer at rest. The three-dimensional locations of the markers attached to the subjects during scans were measured using an optical motion-tracking system. In the phantom study, we performed a transmission scan and seven $^{18}$F emission scans of a baseline and with artificial misalignment of shifts and rotations. The correlation coefficients between the baseline and the other images before and after the corrections for the misalignment were calculated. In the human study, we performed a $^{15}$O-water dynamic scan with a transmission and axially 30 mm-shifted transmission scans. Motion of the subject was estimated by the information from the system, and was corrected on each sinogram using attenuation maps realigned to dynamic frames. Reconstructed dynamic images were then realigned to the transmission data. We calculated rMBF values for nine segments and myocardial images from the emission images, which were reconstructed with the first attenuation map (reference) and with the misaligned attenuation map before and after our corrections.
*Results* In the phantom study, the correlation coefficients were improved from $0.929 \pm 0.022$ to $0.987 \pm 0.010$ (mean $\pm$ SD) after the corrections. In the human study, the global and cyclic movements were detected. The cyclic movement due to respiration was smoothed by frame-averaging, and reasonable information of the global movement was obtained. The rMBF value (mean $\pm$ SD) was $0.94 \pm 0.12$ mL/min/g for the reference. The rMBF values using the misaligned attenuation map changed from $1.03 \pm 0.21$ to $0.93 \pm 0.11$ mL/min/g after the correction, and spurious defects in myocardial images were also recovered.
*Conclusions* Our technique provided reasonable information for correcting the global movement of the subject. It was shown that this system was applicable to detect and correct subject movement in cardiac PET studies at rest.

**Keywords** Myocardial blood flow · PET · Motion correction · Attenuation correction · $^{15}$O-labeled water

K. Koshino (✉) · H. Watabe · H. Iida
Department of Investigative Radiology,
National Cardiovascular Center Research Institute,
5-7-1 Fujishirodai, Suita, Osaka 565-8565, Japan
e-mail: koshino@ri.ncvc.go.jp

S. Hasegawa
Department of Cardiology, Osaka Koseinenkin Hospital,
Osaka, Japan

T. Hayashi
Functional Probe Research Laboratory,
RIKEN Center for Molecular Imaging Science, Hyogo, Japan

J. Hatazawa
Department of Nuclear Medicine and Tracer Kinetics,
Osaka University Graduate School of Medicine, Osaka, Japan

## Introduction

Motion of a patient during a positron emission tomography (PET) scan can cause deterioration in image quality and quantitative accuracy. Several techniques have been

proposed for motion compensation in neuroimaging [1–7]. In cardiac PET studies, effects of wall contractile and respiratory motion can be smoothed in the temporary sampled PET images, but global movement of the patients during the relatively long scanning period is still a significant source of errors [8–11].

It was shown that misalignment by a 20-mm shift in the lateral/septal direction between transmission and $^{18}$F-fluorodeoxyglucose ($^{18}$FDG) emission scans caused a 30% change in regional activity in cardiac $^{18}$F-FDG PET [8]. To align two $^{18}$F-FDG emission images acquired on different days, Bacharach et al. [11] proposed a registration technique based on the rigid body model using the transmission images by assuming no misregistration between transmission and emission data sets.

Cardiac $^{15}$O-water PET studies provide quantitative information with regard to the viabilities of myocardium using the myocardial blood flow (MBF), coronary flow reserve, and perfusable tissue index [12–19]. Naum et al. [20] demonstrated that the movement occurred during dynamic scans with cycling. They proposed a method to correct for the motion during a single dynamic scan, and among different sessions, by aligning the dynamic frames of $^{15}$O-water images using two external radioactive markers placed on the back of a subject. Although their technique did not provide correction for misalignment between transmission and emission data, reasonable improvement in calculated MBF values was demonstrated.

Correcting the misalignment between the transmission and emission data is a challenging task because the image contrast of transmission images differs from that of emission images. The distribution of $^{15}$O-water also varies dramatically in regions of the right and left ventricles, myocardium, and other organs over time. Additionally, the image quality of PET with $^{15}$O-water is worse than that with other radioligands due to the short half life of $^{15}$O, which makes image registration difficult.

In this paper, we describe a novel approach using an optical motion-tracking system for detecting the subject's global movement during the relatively long study period, as an extension of the early studies of Watabe et al. [4]. The proposed technique provided correction for misalignment between dynamic emission sinograms, and also provided accurate attenuation correction, in which misalignment between attenuation map and each emission sinogram was corrected in the reconstruction stage.

First, the inherent accuracy of our system was evaluated. Then, the system was validated on a cardiac phantom study for artificial misalignment between an attenuation map and emission data. Correction for global movement obtained by monitoring the locations of external markers on chest skin was validated in a $^{15}$O-water cardiac PET study in a healthy volunteer at rest.

## Materials and methods

### Hardware-based position monitoring system

To detect motion of a subject, we adopted an optical motion-tracking device in which targets attached to the chest skin are monitored. The motion compensation approach using an optical motion-tracking system has been previously validated in brain PET studies [3–7]. We applied this approach to the cardiac PET studies. Figure 1a shows an optical motion-tracking system, POLARIS (Northern Digital Inc., Canada). The POLARIS has two charge-coupled-device cameras, and provides the 3D position of a target. The three-dimensional position is measured in the form of 6 degrees of freedom: three rotational angles, and three translational directions. The manufacturer reports that the accuracy of the rotational angle and translation are better than 0.3° and 0.5 mm, respectively. Figure 1b shows a target with four infrared-reflective markers and supporting post. The target and supporting post made of carbon resin were pinned with two fluoroplastic screws. Figure 1c shows the position calibration tool used to convert the locations of subject positions in the POLARIS coordinate into PET coordinates. Figure 1d represents the schematic diagram of our system. Locations of targets attached to the chest skin of the subject and the gantry of a PET scanner were measured with the POLARIS. The target on the gantry of the PET scanner was used as a reference in order to convert the subject's positions from the POLARIS coordinate to the PET coordinate. Figure 1e shows an example of the experimental setup with a healthy volunteer in the cardiac PET study. Two targets were attached to the chest skin of the subject. Three legs of the supporting post were attached to the skin of the subject using surgical tape. The axial field-of-view (FOV) of the PET scanner used in the human study, HEADTOME-V tomography (SHIMADZU Corp., Kyoto, Japan), was 200 mm, and the gantry diameter was 850 mm [21]. The geometries of targets attached to the thoracic surface were $85 \times 85$ mm$^2$ (the left-hand target in Fig. 1e, target 1) and $65 \times 90$ mm$^2$ (the right-hand target in the Fig. 1e). The heights of supporting posts for target 1 and target 2 were 50 and 42 mm, respectively. We calculated the subject's positions in the PET coordinate by measuring the locations of the target with four infrared-reflective markers (the primary target). Another target was used as a reserve in cases when the primary target was hidden from the FOV of the POLARIS.

### Motion correction

The rigid motion correction technique employed is an extension of the previous work for brain PET studies by

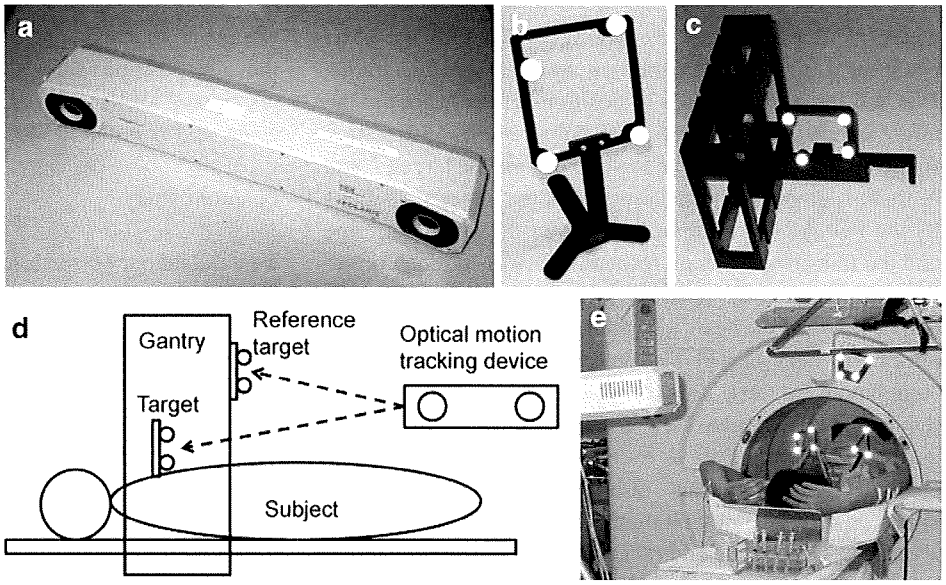


**Fig. 1** Our motion correction system. **a** Optical motion-tracking device. **b** Target consists of infrared-reflective markers with supporting post. **c** Position calibration tool with a target. **d** Schematic diagram of the system. Locations of the targets on the subject and the gantry were measured with the optical motion-tracking device. **e** An example of the experimental configuration

Watabe et al. [4]. We consider four coordinates: the POLARIS $C_S$, a target on a PET gantry for reference $C_G$, a target attached on a subject $C_T$, and the PET scanner $C_P$. By measuring the location and orientation of each target attached to the subject and the gantry using the POLARIS, we obtained a 4 × 4 transformation matrixes, $T_{T\to S}$ from $C_T$ to $C_S$, and $T_{G\to S}$ from $C_G$ to $C_S$, respectively. Motion matrix $M_{P_1\to P_2}$ from a position $P_1 = P(t_1)$ to another position $P_2 = P(t_2)$ in the PET coordinate is written as follows [4]:

$$M_{P_1\to P_2} = T_{G\to P}T^{-1}_{G\to S}T_{T_1\to S}T^{-1}_{T_2\to S}T_{G\to S}T^{-1}_{G\to P} \quad (1)$$

where $T_1$ and $T_2$ are positions in target coordinates corresponding to positions $P_1$ and $P_2$ in the PET coordinate. $T_{G\to P}$ is the matrix to transform a position from the gantry coordinate to the PET coordinate. The matrix is given by the following equation:

$$T_{G\to P} = T_{S\to P}T_{G\to S} \quad (2)$$

$T_{S\to P}$ is the matrix which relates the POLARIS and PET coordinates and is obtained by position calibration.

The point source was embedded in a given position of a target, which is fixed on the calibration tool shown in Fig. 1c. By measuring the position of the point source using the POLARIS, the position $P_S = (x_S, y_S, z_S)$ of the point source in the POLARIS coordinate is calculated using the known position $P_T = (x_T, y_T, z_T)$ in the target coordinate and $T_{T\to S}$, as $P_S = T_{T\to S}P_T$. The position $P_P = (x_P, y_P, z_P)$ in the PET coordinate is also obtained from the reconstructed emission image. By changing the position of the target, in which the point source is embedded, $T_{S\to P}$ is calculated using the least-squared-fit between the pairs of $P_S$s and $P_P$s. The PET coordinate was

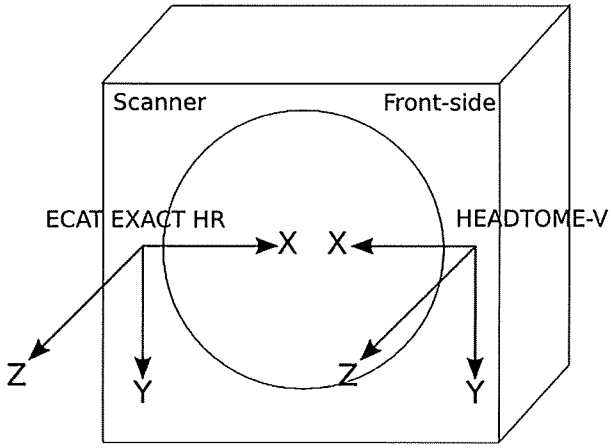


**Fig. 2** PET coordinates defined by position calibrations

defined by the position calibration as shown in Fig. 2. The positions of subjects in the PET coordinate will be discussed in the following.

To correct a subject's movements during a dynamic acquisition of an emission scan with multiple frames, we estimated the heart locations from the locations of the target, which are measured by the POLARIS. The displacement of the COG of the heart's position from during the transmission scan to during each dynamic frame of the emission scan is given by

$$\begin{aligned} H^F - H^{TCT} &= \frac{1}{L}\sum_t^F H(t) - \frac{1}{N}\sum_t^{TCT} H(t) \\ &= \frac{1}{L}\sum_t^F [P(t) + \Delta(t)] - \frac{1}{N}\sum_t^{TCT} [P(t) + \Delta(t)] \end{aligned} \quad (3)$$

where $H^{TCT}$ and $H^{F}$ are the averaged COGs of the heart positions during the transmission and the dynamic frame, $H(t)$ and $P(t)$ are the COGs of positions of the heart and the target at time $t$, $\Delta(t)$ is a term representing a non-rigid relation for positions at time $t$ between the heart and the target, $L$ and $N$ are the numbers of measurements of the target's positions by the POLARIS during acquisition of the dynamic frame and the transmission scan, respectively. For motion correction, we assumed the rigid body model, in which the target and the COG of the heart's position have linear movement at least in the FOV of a PET scanner, that is, we assumed that summations of $\Delta(t)$ for the transmission scan and the dynamic frame equal to zero. The procedures of our motion-correction technique are as follows: (1) An attenuation map is aligned to the coordinate of a dynamic frame of an emission scan using the motion matrix in Eq. 1, in which $P_1$ and $P_2$ are $\Sigma^{TCT}P(t)/N$ and $\Sigma^{F}P(t)/L$ in Eq. 3. (2) The attenuation map is then converted to its sinogram by forward projection. (3) Each sinogram of the dynamic frames is reconstructed with the realigned attenuation sinogram. (4) The emission image is aligned to the transmission coordinate with the inverse matrix of the motion matrix. (5) Last, procedures from 1 through 4 are repeated for all dynamic frames of the emission data.

## Position calibrations

Position calibrations were performed on two PET scanners to obtain a matrix $T_{G\to P}$ in Eq. 2, which transforms the subject's positions from a gantry coordinate to a PET coordinate. For ECAT EXACT HR tomography (CTI/Siemens, Knoxville, TN, USA) [22] used in a cardiac phantom study, ten emission scans were performed, each displaying different positions of a radioactivity point source of $^{18}$F solution, using the calibration tool in Fig. 1b. For the PET scanner used in a healthy volunteer study, 14 emission scans were performed with the $^{18}$F solution point source and calibration tool.

The accuracy of the calibrations was evaluated from $T_{G\to S}$ and $T_{S\to P}$ in Eq. 2. The accuracy of $T_{G\to S}$ part was evaluated by determining the standard deviation (SD) of rotational angles and translations calculated from position data of the gantry, because $T_{G\to S}$ depends on only the accuracy of the measurements in regard to the POLARIS. To evaluate the accuracy of $T_{S\to P}$ part, we calculated errors between a position of a point source $P_P$, and the approximation position using $T_{S\to P}$, $P_X = T_{S\to P}P_S$:

$$e(i,k) = P_X(i,k) - P_P(i,k) \tag{4}$$

$$\mathrm{RMSE}(i) = \sqrt{\sum_{k=x,y,z} |P_X(i,k) - P_P(i,k)|^2} \quad (k = X, Y, Z \text{ and } i = 1, \ldots, N) \tag{5}$$

where $e(i, k)$ is the approximation error of a point source in the $i$th position for each direction, $X$, $Y$, and $Z$ are orthogonal axes in Fig. 2, RMSE($i$) is the root mean square error, and $N$ is the number of positions of a point source.

## Phantom study

To validate our correction technique for the misregistration between the attenuation map and emission data, we performed PET scans using a cardiac phantom (KYOTO KAGAKU co., LTD, Kyoto, Japan, type HL-D) and the ECAT EXACT HR tomography. The phantom mimics the human thoracic region and has cardiac and liver inserts. The insert can be filled with radioisotope solution. The myocardium and liver inserts were filled with the $^{18}$F solution of relative activities of 1 and 4. A target (without the supporting port) for the POLARIS was attached to the phantom using polyethylene cross tape. Then, we performed a 1,000-s transmission scan for attenuation corrections. After the transmission scan, seven $^{18}$F emission scans were performed with a set of single frame data for 180 s. The first scan was the baseline (scan #1), in which there was no misalignment to the transmission. For the following three emission scans (scan #2–4), the phantom was moved in the $X$, $Y$, and $Z$ directions. For the other three scans, the phantom was rotated about the $X$, $Y$, and $Z$ axes (scan #5–7). The phantom's positions were measured with the POLARIS.

The reconstructed images before and after the correction were obtained using an FBP (filtered back-projection) algorithm with a Gaussian filter of 6 mm FWHM (full-width at half-maximum). The matrix size and voxel size of images were 128 × 128 × 47 and 4.4 × 4.4 × 3.1 mm$^3$, respectively. All emission data were corrected for physical decay of $^{18}$F with base time as the start of the first emission scan, and all of the emission images were reoriented to the short axis using a transformation matrix.

To evaluate the effects of the corrections, we calculated correlation coefficients for myocardial regions between the baseline and misaligned emission images, both before and after the corrections.

## Human study

A cardiac $^{15}$O-water PET study was performed on a healthy volunteer (male, 32 years old) using the HEADTOME-V tomography in order to validate use of the external markers on the chest skin and also to evaluate the effects of the global movement on the quantification of MBF by artificial misalignment between attenuation and emission data. The healthy volunteer gave written informed consent according to a protocol approved by the Ethical Committee and

Internal Review Board of Osaka University. The PET study consisted of a 20-min transmission scan, an 8-min $^{15}$O-CO emission scan for blood pool imaging, a 6-min $^{15}$O-water emission scan with 26 dynamic frames (12 × 5, 8 × 15 and 6 × 30 s), and a second 20-min transmission scan. All scans were acquired in a 2D acquisition mode. The radioactivity of inhaled $^{15}$O-CO gas was 3.2 GBq. $^{15}$O-water was injected via the left brachial vein; activity was 1.1 GBq for 40 s. All scans were performed without pharmacological stress. To investigate the accuracy of the POLARIS for tracking the locations of the target attached to the thorax skin of the subject, the couch of the PET scanner was moved +30 mm along the axial direction before the second transmission scan, corresponding to the $Z$ direction in Fig. 2, with the subject lying on the couch. It was expected that the shift in the $+Z$ direction caused the artificial deterioration of image quality and quantitative accuracy in especially the anterior and lateral regions. The subject's positions during the scans were monitored by the POLARIS, at a frequency of one sample per second.

The reconstructed images for the four cases were obtained using an FBP algorithm with a Gaussian filter of 9 mm FWHM. The matrix and voxel sizes of the reconstructed images were 128 × 128 × 63 and 2.03 × 2.03 × 3.13 mm$^3$. No scatter correction was performed during the image reconstruction stage.

Regional MBF values were estimated for four cases. Case 1: the first attenuation map and emission data, case 2: the first attenuation map and emission data with correction for the subject's motions, case 3: the second attenuation map and the emission data, case 4: the second attenuation map and the emission data after the correction for the subject's motions and the 30-mm-shifted misalignment. Differences in the MBF values for cases 1 and 2 were considered to indicate effects from the correction for the frame-averaged motion if the subject's motion was small. Differences in MBF values for cases 1 and 3 could indicate errors in the quantification of MBF caused by the artificial misalignment between the second attenuation map and the emission data. The lack of any difference in MBF values for cases 1 and 4 indicated that our technique tracked the shift of the target on the thorax skin accurately and corrected the misalignment. In order to generate cases 2 and 4, the positions $P_1$ and $P_2^{(j)}$ in Eq. 1 were calculated as averaged COGs of the subject's positions during the first and second transmission scans and the $j$th dynamic frame of $^{15}$O-water or C$^{15}$O emission scan. Using Eq. 1 with $P_1$ and $\{P_2^{(j)}\}$, we performed frame-by-frame motion corrections for all dynamic frames of emission data. Due to the fact that the PET scanner did not provide a dynamic transmission scan, we assumed that the subject did not move during the transmission scan.

For quantification of MBF, we employed a compartment analysis model proposed by Iida et al. [13], which provided corrections for spillover from a left ventricle and partial volume effect and generated a MBF value in units of mL/min/g of perfusable tissue. All transmission and emission images were reoriented to the short axis. To calculate tissue time activity curves, regions of interest (ROIs) were drawn in nine myocardial regions: apical, mid-anterior, mid-lateral, mid-posterior, mid-septal, basal-anterior, basal-lateral, basal-posterior, and basal-septal regions. To avoid spillover effects from the right ventricle, the sizes of ROIs in septal regions were smaller than those in other regions. Another ROI was drawn on the left ventricle in order to estimate the arterial input function [19]. These ROIs were manually and independently drawn for the four cases. In addition, to validate the consistency between the quantitative results of MBF values and the quality of the images, we calculated the build-up and washout phase images [23] for the four cases. The build-up and washout phase images were obtained by subtracting a blood pool image from summed images of early (0–180 s) and later (180–360 s) frames of a $^{15}$O-water image.

We evaluated the magnitude of the subject's motions in the PET coordinate during each scan. We defined position $P_1$ in Eq. 1 as the position at the start of the first transmission scan, and position $P_2$ as the position at an arbitrary time during a transmission or an emission scans. The rotational angles and translations for arbitrary times were obtained using Eq. 1. We represented motion during a scan in the form of mean ± SD for each rotational angle and translation.

## Results

### Position calibrations

Table 1 shows the inherent accuracy of our system in the two PET scanners. Values of SDs for rotations and translations obtained from $T_{G\to S}$ data were very small. Table 1 also shows the approximation errors (mean ± SD) occurred while transforming the positions of a point source from the POLARIS coordinate to the PET coordinate using $T_{S\to P}$. There was no bias in any direction in either scanner. Each value of RMSE was smaller than the spatial resolution of the corresponding scanner [21, 22].

### Cardiac phantom study

Table 2 lists the observed misalignment from the reference position of the phantom in the transmission scan and the correlation coefficients between the reference image and the misaligned images before and after the corrections (mean ± SD; 0.929 ± 0.022 and 0.987 ± 0.010). The

**Table 1** Inherent accuracy of the motion correction system in the two PET scanners

| Scanner | $T_{G\to S}$ | | | | | | $T_{S\to P}$ | | | | # of point positions |
|---|---|---|---|---|---|---|---|---|---|---|---|
| | Rotational angle (deg) | | | Translation (mm) | | | $e_x$ | $e_y$ | $e_z$ | RMSE | |
| | $r_x$ | $r_y$ | $r_z$ | $t_x$ | $t_y$ | $t_z$ | | | | | |
| ECAT EXACT HR | 0.0 | 0.0 | 0.0 | 0.0 | 0.0 | 0.0 | 0.0 ± 0.8 | 0.0 ± 0.9 | 0.0 ± 0.8 | 1.3 ± 0.4 | 10 |
| HEADTOME-V | 0.0 | 0.0 | 0.0 | 0.0 | 0.0 | 0.1 | 0.0 ± 1.5 | 0.0 ± 1.6 | 0.0 ± 0.6 | 2.3 ± 0.2 | 14 |

Standard deviations of rotational angles and translations obtained from $T_{G\to S}$ data and approximation errors (mean ± SD in mm) by transforming positions of a point source from the POLARIS coordinate to the PET coordinate using $T_{S\to P}$. Columns $T_{G\to S}$, $r_x$, $r_y$ and $r_z$ denote SDs of rotational angles about three orthogonal *X*, *Y*, and *Z* axes, respectively. $t_x$, $t_y$ and $t_z$ denote SDs of translations along three orthogonal axes, respectively. Columns $T_{S\to P}$, $e_x$, $e_y$, and $e_z$ denote average values (mean ± SD in mm) of $e(i, X)$, $e(i, Y)$, and $e(i, Z)$, respectively. $e(i, k)$ was defined in Eq. 4. *RMSE* denotes an average value (mean ± SD in mm) of *RMSE*(*i*), defined in Eq. 5

**Table 2** The observed misalignment and correlation coefficients for the phantom study

| Scan no. | Rotation (deg) | | | Translation (mm) | | | Correlation coefficient | |
|---|---|---|---|---|---|---|---|---|
| | $r_x$ | $r_y$ | $r_z$ | $t_x$ | $t_y$ | $t_z$ | Before MC | After MC |
| 2 | 0.0 | 0.2 | 5.1 | 35.7 | 0.8 | −3.4 | 0.896 | 0.997 |
| 3 | 0.0 | −1.0 | 1.3 | 0.9 | 35.2 | 3.2 | 0.938 | 0.995 |
| 4 | 0.0 | −0.2 | 0.9 | 5.9 | 0.1 | 42.8 | 0.917 | 0.971 |
| 5 | 13.1 | 1.4 | 0.4 | 1.9 | 22.5 | 17.1 | 0.926 | 0.986 |
| 6 | 2.4 | −15.6 | −2.1 | 10.9 | 3.8 | 4.7 | 0.938 | 0.982 |
| 7 | −0.6 | 1.8 | −13.5 | 13.4 | 11.9 | −9.5 | 0.960 | 0.992 |

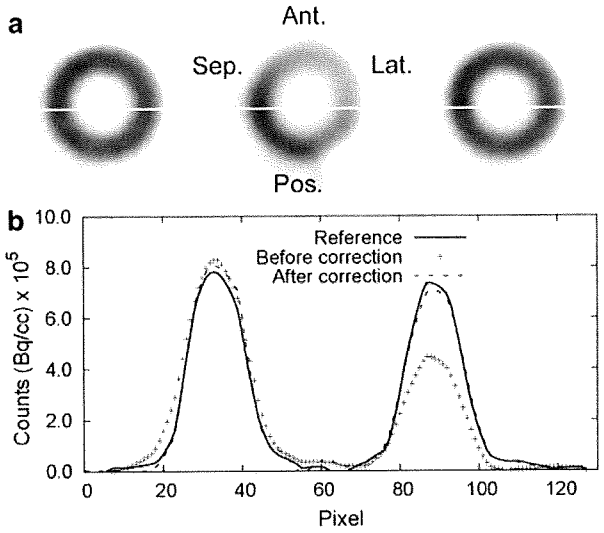


**Fig. 3** Reconstructed and reoriented images of the phantom. **a** Reconstructed images. *Left*, *mid*, and *right* columns represent the reference emission image (no misalignment), the second emission images before correction for misalignment, and the second emission images after correction for the misalignment, respectively. **b** Profiles at the level of white lines in images. *Solid line*, *cross symbols*, and *dashed lines* represent the first emission image, the second emission images before correction, and the second emission images after correction, respectively

effects of our correction technique are demonstrated in Fig. 3. The left column in Fig. 3a is the reference emission image (no misalignment). The middle and right columns represent the emission images with the misalignment of the *X*-direction before and after the corrections. For the image in the middle column, only the position was transformed to the transmission coordinate after the reconstruction. Figure 3b represents line profiles at the level of white lines in the slices.

## Human study

Table 3 summarizes the observed movements of the subject during scans relative to the beginning of the first transmission scan, in the form of rotational angles about and translations along three orthogonal axes. It was observed that the magnitude of the average parts of the rotational angles and translations tended to increase. The value of $t_z$ changed from −1.8 ± 0.6 to 28.3 ± 0.6 mm between the $^{15}$O-water emission and the second transmission scan mainly because of the 30-mm shift of the couch as well as the motions of the subject. There was little change in the SD in any rotational angle or translation among the scans.

Figure 4 shows motion parameters during $^{15}$O-water scan. Figure 4a and b represent the sample-by-sample and frame-averaged translations. Figure 4c and d shows the sample-by-sample and frame-averaged rotational angles.

Table 4 shows that the MBF values (mean ± SD), which were obtained from nine myocardial segments, were 0.94 ± 0.12, 0.91 ± 0.13, 1.03 ± 0.21, and 0.93 ± 0.11 mL/min/g for the four cases. The values for cases 1 and 2 were obtained from the emission data and the first attenuation map before and after motion correction. The values for cases 3 and 4 were obtained from the emission data and the second attenuation map before and after the corrections for the subject's motions and the 30-mm shift of the couch. There were significant

**Table 3** Observed movements (mean ± SD) of the healthy volunteer during scans relative to the beginning of the first transmission scan

| Scan | Rotational angle (deg) | | | Translation (mm) | | |
|---|---|---|---|---|---|---|
| | $r_x$ | $r_y$ | $r_z$ | $t_x$ | $t_y$ | $t_z$ |
| TCT 1 | −0.1 ± 0.2 | −0.4 ± 0.2 | −0.2 ± 0.2 | 0.7 ± 0.5 | 1.3 ± 0.6 | 1.0 ± 0.8 |
| $C^{15}O$ | 0.0 ± 0.2 | −0.1 ± 0.2 | −0.7 ± 0.1 | 2.6 ± 0.3 | 1.0 ± 0.5 | −1.7 ± 0.7 |
| $^{15}O$-water | 0.4 ± 0.2 | 0.0 ± 0.1 | −0.7 ± 0.1 | 2.7 ± 0.2 | 1.3 ± 0.4 | −1.8 ± 0.6 |
| TCT 2 | −0.4 ± 0.2 | 0.7 ± 0.2 | −2.0 ± 0.1 | 3.7 ± 0.3 | 2.6 ± 0.5 | 28.3 ± 0.6 |

$r_x$, $r_y$, and $r_z$ denote rotational angles (degrees) about X, Y, and Z-axes, respectively. $t_x$, $t_y$, and $t_z$ denote translations (mm) along $X$, $Y$, and $Z$ axes, respectively

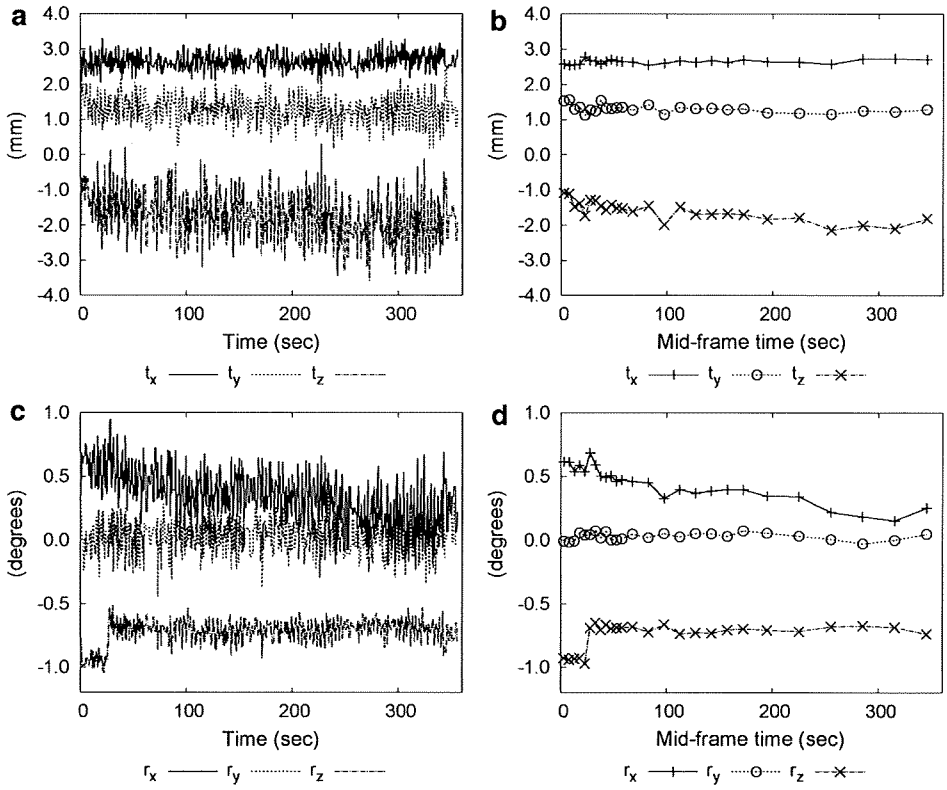


**Fig. 4** Motion parameters during $^{15}O$-water study on the healthy volunteer. **a**, **b** Sample-by-sample and frame-averaged translations. **c**, **d** Sample-by-sample and frame-averaged rotational angles

**Table 4** MBF values (mL/min/g of perfusable tissue) of the healthy volunteer

| Myocardial region | Case | | | |
|---|---|---|---|---|
| | 1 | 2 | 3 | 4 |
| Apical | 1.05 | 1.00 | 0.99 | 1.05 |
| Mid-anterior | 0.92 | 0.89 | 1.26 | 0.99 |
| Mid-lateral | 0.93 | 0.89 | 1.38 | 0.89 |
| Mid-posterior | 1.14 | 1.16 | 0.96 | 1.01 |
| Mid-septal | 1.05 | 1.06 | 1.08 | 1.12 |
| Basal-anterior | 0.87 | 0.80 | 1.18 | 0.80 |
| Basal-lateral | 0.86 | 0.82 | 0.95 | 0.84 |
| Basal-posterior | 0.88 | 0.83 | 0.84 | 0.86 |
| Basal-septal | 0.73 | 0.72 | 0.65 | 0.82 |
| Mean ± SD | 0.94 ± 0.12 | 0.91 ± 0.13 | 1.03 ± 0.21 | 0.93 ± 0.11 |

differences in the mid-anterior and mid-lateral regions as well as the basal-anterior regions between cases 1 and 3.

Figure 5 demonstrates the influence of misalignment between an attenuation map and emission data on the quality of myocardial images, as well as the effect of our correction technique. Figure 5a–f represent the build-up and washout phase images of middle myocardial obtained from the $^{15}O$-water data. Anterior, lateral, posterior, and septal regions of myocardia were arranged in a clockwise manner. Figure 5a and e was obtained from the data of case 1, and Fig. 5b and f was calculated from the data obtained in case 2. Figure 5c and g was derived from the data in case 3, and only positions of reconstructed images were transformed to the first transmission coordinate after reconstructions for visual